Chiang Mai J. Sci. 2018; 45(4) : 1843-1854
http://epg.science.cmu.ac.th/ejournal/
Contributed Paper

Highly-sensitive and Selective Nitric Oxide Sensor Based on Electrolytically Exfoliated Graphene/Flame-spay-made SnO_2 Nanocomposite Films

Nantikan Tammanoon [a,b], Anurat Wisitsoraat [c], Chakrit Sriprachuabwong [c], Ditsayut Phokharatkul [c], Adisorn Tuantranont [c], Sukon Phanichphant [d] and Chaikarn Liewhiran* [a,d]

[a] Department of Physics and Materials Science, Faculty of Science, Chiang Mai University, Chiang Mai 50202, Thailand.

[b] Graduate School, Chiang Mai University, Chiang Mai 50202, Thailand.

[c] Nanoelectronics and MEMS Laboratory, National Electronics and Computer Technology Center, National Science and Technology Development Agency, Klong Luang, Pathumthani 12120, Thailand.

[d] Materials Science Research Center, Faculty of Science, Chiang Mai University, Chiang Mai 50202, Thailand.

* Author for correspondence; e-mail: chaikarn_l@yahoo.com

Received: 23 March 2017
Accepted: 17 May 2017

ABSTRACT

In this work, 0-5wt % electrolytically exfoliated graphene/flame-spray-made undoped SnO_2 nanocomposites were systematically studied for NO sensing at low working temperatures. Characterizations by X-ray diffraction and transmission/scanning electron microscopy demonstrated that multilayer graphene sheets were widely distributed within spheriodal nanoparticles having polycrystalline tetragonal SnO_2 phase. The sensing films fabricated by powder pasting and spin coating techniques were tested toward 0.125-5 ppm NO at temperatures ranging from 25°C to 350°C in dry air. Gas-sensing results showed that the optimal graphene loading level of 0.5 wt% provided an ultrahigh response of ~7,275 toward 5 ppm of NO and good recovery stabilization at a low optimal operating temperature of 200°C. Furthermore, the sensors displayed high NO selectivity against NO_2, H_2, C_3H_6O, H_2S and CH_4. Therefore, the electrolytically exfoliated graphene-loaded FSP-made SnO_2 sensor is a highly promising candidate for sensitive and selective detections of NO in biomedical diagnostic applications.

Keywords: flame spray pyrolysis, nitric oxide, SnO_2, graphene loading, gas sensor

1. INTRODUCTION

Nitric oxide (NO) is a greenhouse gas produced from the combustion of fossil fuels and is a key component of photochemical smog, which causes eye irritation and respiratory problems [1].It is thus crucial to determine atmospheric NO concentration for assessment of the smog severity in order to provide rapid public warning and corrective actions. In addition, NO is present in breath due to its biological functions and NO

concentration can be used for diagnosing respiratory diseases [2]. For instance, 22-44 ppb of NO in exhale breath indicates chronic asthma conditions [3]. Therefore, NO sensors with very high sensitivity and fast response are required for human health diagnosis.

Metal oxide semiconductors such as tin oxide (SnO_2), tungsten oxide (WO_3) and zinc oxide (ZnO) are potential candidates for various gas sensing applications because of their stable chemical transduction properties, fast response and simple electronic interface [4]. Particularly, tin dioxide (SnO_2), a direct wide band gap (E_g= 3.67 eV at 300 K) *n*-type semiconductor, is most commonly used in commercial gas-sensing applications due to its low cost, diverse gas reactivity, moderate electrical conductivity and good stability [5]. However, it still exhibits limited response and selectivity towards particular gases at nominal working temperatures of 200-450°C. Various additives including transition metal, metal oxide and carbon nanostructures have been extensively studied to improve the gas-sensing performances of SnO_2. Among these, graphene, a new atomically thin carbon material, has recently emerged as an effective additive for the gas-sensing enhancement of metal oxide sensors because of its large specific surface area, strong interaction with electron donating or accepting gas molecules adsorbed on its surface, high conductivity and low price [6-7].

NO-sensing performances of various nanomaterials prepared by different synthetic methods are summarized in Table 1. Firstly, Pd-decorated WO_3/SnO_2 double layer sensors prepared by screen printing showed a good response of 38 to 200 ppm NO at 400°C [8]. Similarly, 1.0 at% Sb-doped Sn_2O_3 gas sensors fabricated via a facile hydrothermal technique exhibited a decent response ~45.7 to 600 ppm NO at 200°C [9]. In addition, crystalline SnO_2nanopowders and thin films made by sol-gel and spin-coating techniques displayed a fair response of ~3.1 to NO 495 ppm with fast response/recovery behaviors at 350°C [10]. Also, ultra small SnO_2 nanocrystals synthesized by the biuret-assisted hydrothermal method revealed an excellent response to NO at 300°C of 1.2 for 0.1 ppm, 1.8 for 1 ppm, 119.5 for 5 ppm, 864.5 for 20 ppm, 991 for 30 ppm, 1173 for 50 ppm and 1187 for 100 ppm, respectively [11]. Additionally, 0.2wt% Co-doped SnO_2 nanoparticles synthesized by flame spray pyrolysis (FSP) was reported to offer a high response of 1637 to 1000 ppm NO at 350°C [12]. Moreover, Pt nanoparticle-reduced graphene oxide nanohybrid exhibited a response of 1.11 (1.09)to 1000 ppm NO, respectively with (without) Pt nanoparticles at room temperature [13]. Furthermore, chemically synthesized 0.2 wt% copper-ion-doped (Cu^{2+}) PANI/WO_3composite films coated on surface acoustic wave resonators as room temperature nitric oxide sensors displayed a high response of 59 to 80 ppb NO [1]. Likewise, zinc oxide (ZnO) decorated graphene oxide (GO) sheets fabricated by Modified Hummer's method and Sonochemical synthesis exhibited a sensor response of 1.035 to 5 ppm NO at room temperature [14]. Furthermore, 10 wt% Pd-loaded Co_3O_4 prepared by a colloidal mixing method showed a sensor response of 1.16 at 50 ppb NO at 200°C [15].

Table 1. Summary of NO-Sensing performances of various nanomaterials prepared by several synthetic methods toward VOCs.

Sensing materials	Synthesis	Temp.	Response& Conc.	Reference
0.2 wt%Cu^{2+} doped PANI/WO_3	Sol-gel and chemical polymerization	R.T.	59, 80 ppb	Wang *et al.*[1]
1 at% Sb/Sn_2O_3 nanoparticles	Facile hydrothermal method (powders)/ Spin-coating (sensors)	200°C	45.7, 600 ppm	Zhao *et al.*[9]
SnO_2 nanoparticles	Sol-gel method (powders)/ Spin-coating (sensors)	350°C	3.1, 495 ppm	Canevali *et al.*[10]
SnO_2	Hydrothermal	300°C	119.5, 5 ppm	Lv. *et al.*[11]
0.2 wt% Co/SnO_2	FSP (powders)/ Spin-coating (sensors)	350°C	1637, 1000 ppm	Punginsang *et al.*[12]
RGO-Pt nanoparticles	Modified Hummer's method	R.T.	1.11, 1000 ppm	Wang *et al.*[13]
ZnO-RGO	Modified Hummer's method and Sonochemical synthesis	R.T.	1.035, 5 ppm	Singh *et al.*[14]
30 wt% Pd-loaded Co_3O_4	colloidal mixing method	200°C	1.16, 50 ppb	Akamatsu *et al.*[15]
0.5 wt% graphene -SnO_2	FSP/ electrolytic exfoliation	200°C	7275, 5 ppm	Present work

Based on these studies, metal oxide sensors prepared by FSP display particularly high NO response and the combination of graphene and metal oxide is a promising approach to high performance NO sensors. FSP is an attractive method for production of metal-doped/loaded metal oxide nanoparticles with large specific surface area in a single high-temperature step. Recently, FSP-made SnO_2 nanoparticles have been combined with graphene synthesized by electrolytic exfoliation, which is a new single-step graphene synthesis method. The resulting SnO_2-graphene composite demonstrates high sensing performances towards some specific gases including ethanol, acetone and NO_2 [16, 17]. Besides, SnO_2 nanoparticles-reduced graphene oxide nanocomposites prepared by chemical oxidation and reduction have shown NO_2-sensing capability at low operating temperatures. However, SnO_2 nanoparticles-graphene composites have not been studied for NO sensing [18]. In this work, electrolytic exfoliated graphene/FSP-made SnO_2 nanocomposites are systematically investigated for selective detection of NO by varying graphene concentrations and operating temperature.

2. MATERIALS AND METHODS

2.1 Synthesis of SnO_2 Nanoparticles and Graphene

Undoped SnO_2 nanoparticles were

synthesized by the FSP method reported previously [16, 17]. Briefly, the precursor solution (0.50 M) prepared by dissolving appropriate amounts of 2-ethylhexanoate (Sigma-Aldrich, 95%) in the 80/20 vol% mixture of xylene (CarloErba, 98.5%)/ acetonitrile (Lab-scan, 99.7%) was sprayed into a premixed oxygen/methane flame under 5/5 condition at 1.5 bar pressure drop across the nozzle tip. Precursor droplets were evaporated and subsequently combusted to form SnO_2 nanoparticles by nucleation, condensation, coagulation, and coalescence. The flame exhibited yellowish orange appearance with a height of ~10 cm. Finally, the as-prepared nanopowder (P-0) was collected on a glass microfibre filter with an aid of a vacuum pump. While, graphene (G) was synthesized by the electrolytic exfoliation process reported recently [8, 9]. In brief, a constant potential of 8V was applied between two graphite rods (1/4" dia, Electron Microscopy Science) immersed in 0.1 wt% of poly(styrenesulfonate) (PSS) (Sigma-Aldrich) electrolyte solution for 7 days to yield high-density graphene dispersion. After that, large graphite agglomerates were centrifuged at 1200 rpm. Finally, the portion of supernatant was selected, washed in distilled water and dried at 80°C to obtain the graphene powder.

2.2 Preparation of Sensing Films

The $SnO_2$and graphene nanopowders were mixed in the binder solution comprising ethyl cellulose (Fluka, 30-70 mPa×s) and α-terpineol (Aldrich, 90%). They were then crushed in a mortar for 30 min to form a homogeneous paste for spin coating. The resulting paste was spin-coated at 3000 rpm for 30 s on Al_2O_3 substrates (0.40 cm × 0.55 cm × 0.04 cm) equipped with interdigitated Au electrodes. Finally, the samples were annealed at 450°C for 2 h in a furnace for binder removal prior to the sensing test.

2.3 Particle and Sensing Film Characterizations

The crystal structure of powder and sensing films were analyzed by X-ray diffractometer (GI-XRD) (RigakuTTRAX III) with a Cu Kα radiation source (30 kV, 15 mA) (JEOL JDX- 3530) detected with a scanning speed of 3°/min. The structural morphologies and accurate size of nanoparticles and sensing films were examined by high-resolution transmission electron microscopy (HR-TEM, TEM: JSM-2010, JEOL) and scanning electron microscopy (SEM: JSM-6335F, JEOL).

2.4 Gas-sensing Measurement

The gas-sensing performances of oxide sensing films were characterized towards NO over the concentration range 0.125-5.0 ppm under atmospheric conditions by the standard flow through technique in a sealed stainless steel chamber at operating temperatures ranging from room temperature of 25 to 350°C. The sensing films were heated to different operating temperatures using an external NiCr heater with a regulated DC power managed by a proportional-integral temperature controller. A constant flux of synthetic dry air was flowed to mix at a standard T-junction with the desired concentration of pollutants dispersed in synthetic air at a constant total flow rate of 2 L/min. The gas flow mixing rates were precisely and rapidly manipulated using computer-controlled multichannel mass flow controllers (Brook Instruments model 5850E). The sensors were exposed to a gas sample for ~10 min at each gas concentration and the pure synthetic air was then restored for 25 min. For *n*-type conductivity, the sensor response (*S*) is

defined as the resistance ratio R_a/R_g, where R_a is the original baseline of resistance in dry air and R_g is the stabilized change in resistance in the reducing gas including C_3H_6O, H_2, H_2S and CH_4. The response definition is reversed for oxidizing gas such as NO, NO_2 and for *p*-type conductivity. The response time (t_{res}) is defined as the time required until 90% of the response signal is reached while the recovery time (t_{rec}) denotes the time needed until 90% of the original baseline signal is recovered.

3. RESULTS AND DISCUSSION

3.1 Structural Properties of FSP Made Powders and Sensing Films

The phase composition and crystallinity of graphene, pure SnO_2, 0.1 to 5 wt% graphene-loaded SnO_2 (G, P-0, P-0.1G to P-5G) nanopowders after annealing in air at 450°C were analyzed by XRD as shown in Figure 1(a). It is seen that electrolytically exfoliated graphene is highly crystalline displaying only two peaks well-matched with (0 0 2) and (0 0 4) planes of graphite-2H-C structure (JCPDS file No. 41-1487(%)) while the undoped SnO_2 nanopowder exhibits the polycrystalline structure of SnO_2 cassiterite-tetragonal phase (JCPDS file no. 41-1445(%)). The full-width-at-half-maximum (FWHM) of (0 0 2) graphene peak is 0.37°, which is comparable with other reports of multi-layer graphene and slightly larger than the value of typical graphite [19]. After loading with 0.1-5 wt% graphene, the diffraction patterns are seen to be insignificantly different from the one with nographene. The result is understandably due to the overlapping between (0 0 2) and (0 0 4) peaks of graphene and (1 1 0) and (2 2 0) peaks of cassiterite SnO_2. In addition, the graphene contents are so low that the change in relative peak intensities are not evident. Figure 1(b) shows XRD patterns of the corresponding sensing films on Au/Al_2O_3 substrates after annealing and sensing test. It can be seen that the sensing films exhibit the same peak locations as their corresponding powders but with relatively low magnitudes compared with those of the Al_2O_3 substrate (JCPDS file No. 46-1212) and Au electrodes (JCPDS file No. 04-0784) because of relatively low amounts of sensor materials.

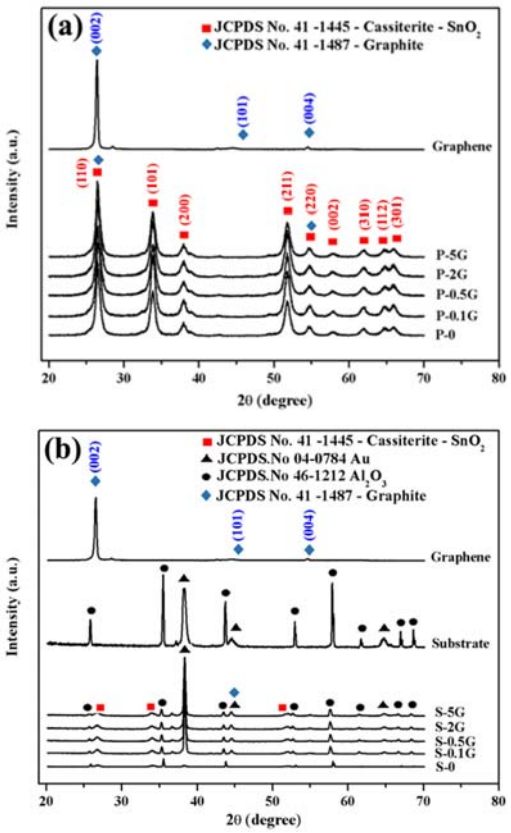

Figure 1. XRD patterns of graphene, pure SnO_2, 0.1 to 5 wt% graphene-loaded SnO_2 (a) powders (G, P-0, P-0.1G to P-5G) and (b) fabricated sensing films (S-0 and S-5G) after annealing and sensing test.

Figure 2 demonstrates a typical BF-TEM image with corresponding SAED pattern and HR-TEM images of 0.5 wt % graphene-loadedSnO_2 nanoparticles (P-0.5G) after binder removal annealing in air at 450°C. It is seen that the polyhedral SnO_2

nanoparticles with diameters of 5-20 nm are randomly dispersed on polygonal graphene sheets with various shapes and sizes, which are partially overlapped among themselves (Figure 2(a)). The corresponding SAED pattern (inset) indicate that the nanostructures are mainly polycrystalline with primary diffraction rings identified as (1 1 0) and (1 0 1) planes of tetragonal-cassiterite SnO_2 phase in good agreement with dominant crystallographic orientations previously observed from XRD data. The HR-TEM image focusing on the nanoparticles (Figure 2(b)) reveals the lattice fringes corresponding to the observed dominant planes in the SAED pattern. In the region around an edge of graphene (Figure 2(c)), few nanoparticles are seen to situate on 7-9 graphitic fringes with the *d*-spacing of 0.419 nm, confirming the decoration of SnO_2 nanoparticles on multilayer graphene structures.

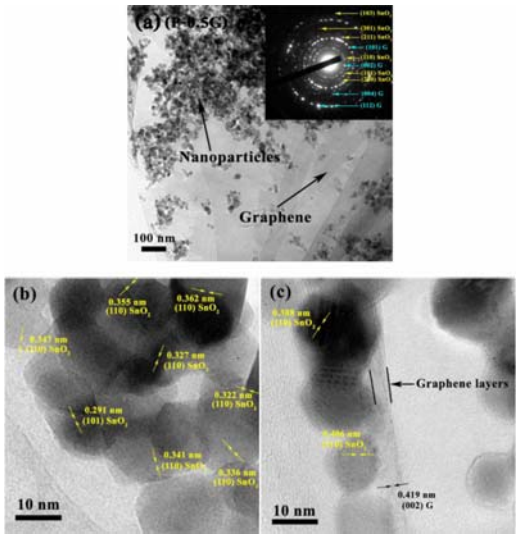

Figure 2(a) BF-TEM, (b) and (c) HR-TEM images of SnO_2 nanoparticles loaded with 0.5 wt % graphene (P-0.5G). Inset: (a) the corresponding SAED patterns.

Figure 3 demonstrates Raman spectra of electrolytically exfoliated graphene and corresponding graphite source. It is seen that graphene exhibit relatively broad G peak at ~1574 cm^{-1}, markedly high D peak at ~1330 cm^{-1} and relatively pronounced 2D band at ~2648 cm^{-1} compared with those of graphite. In addition, a weak D' shoulder associated with disorder defects appear at ~1620 cm^{-1}. These characteristics indicate defective sp^2 lattice, substantial edge defects and moderate second-order zone-boundary symmetry of graphene structure having the number of sp^2 layers in the range of 5-10 [20]. Thus, the electrolytically exfoliated graphene exhibits satisfactory quality in term of number of sp^2 layers but rather low quality in the aspect of crystallinity due to the substantial amount of structural detects. However, the defects have been suggested to be beneficial for gas sensing [21].

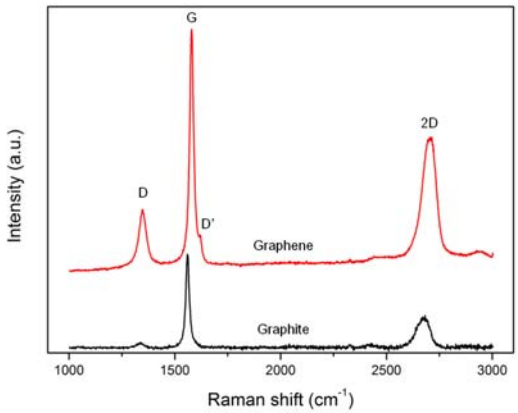

Figure 3. Raman spectra of graphite and electrolytically exfoliated graphene.

Figure 4 illustrates typical top-view SEM micrographs of graphene loaded with graphene at concentration from 0, 0.5 and 5wt% (P-G, P-0, P-0.5G and P-5G) (left) and cross-sectional SEM micrographs of

corresponding sensing films on Au/Al_2O_3 substrates after annealing and sensing test (right). For graphene powder (Figure 4(a)), it comprises several polygonal sheets with varying dimensions in different orientations from a few hundred nanometers to several microns. In addition, many graphene sheets are seen to agglomerate or stack together due to well-known van der Waals interaction. In the case of unloaded SnO_2 powder (Figure 4(b)), it contains mainly nanoparticles with small diameters of less than 30 nm. With 0.5 wt% graphene loading (Figure 4(c)), few of isolated graphene sheets are seen to embed within nanoparticles. At the high graphene content of 5 wt%, more graphene sheets are clearly distributed on the surface (Figure 4(d)). For the corresponding sensing films (Figure 4(e-h)), they have similar thicknesses of ~15-20 μm and become more porous with the inclusion of graphene sheets. Furthermore, more large voids appear within the film at a higher graphene loading level due possibly to distinct thermal expansion coefficients between large grains of graphene sheets and small grains of SnO_2 nanoparticles.

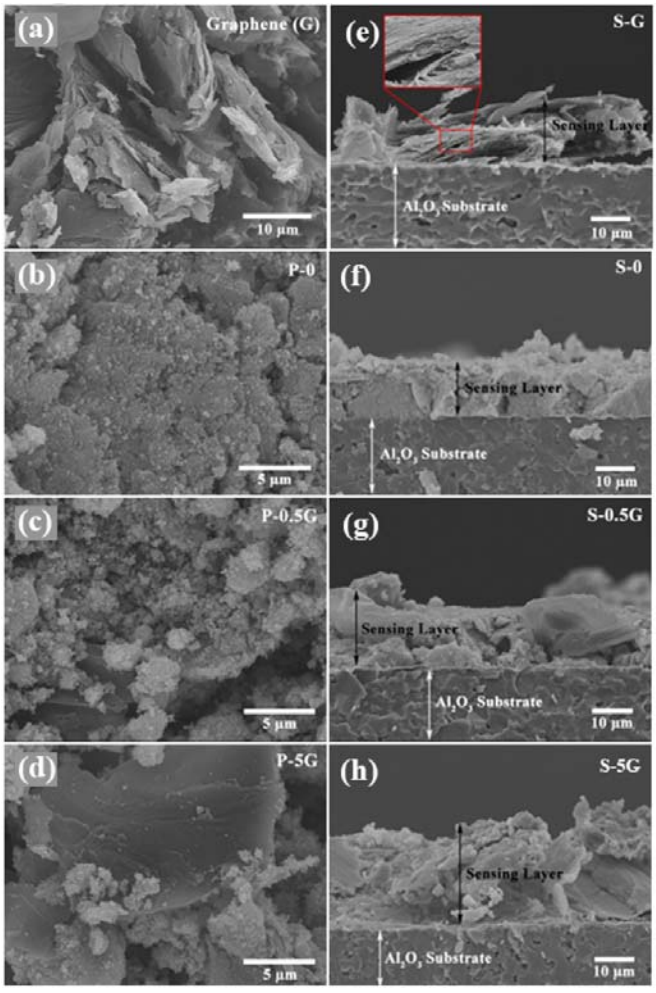

Figure 4. SEM top-view images of (a) G, (b) P-0, (c) P-0.5G and (d) P-5G and SEM cross-sectional-view images of (e) S-G, (f) S-0, (g) S-0.5G and (h) S-5G on Au/Al_2O_3 substrate after annealing and sensing test.

3.2 Gas Sensing Properties

The response of SnO_2 nanoparticles with different graphene loading concentrations to 5 ppm NO at various operating temperatures ranging from 25 to 350 °C are shown in Figure 5. It demonstrates that the NO responses of all sensors elevate greatly as the operating temperature increases from 25 to 200°C and then become steadily declining as the temperature rises further to 350°C. Regarding the impact of graphene content, NO response increases considerably when the graphene loading level increases from 0 to 0.5 wt % and then decreases slowly as the loading content increases further. Especially, the 0.5 wt % graphene-loaded SnO_2 sensor (S-0.5G) offers the highest response of 7,275 to 5 ppm NO at the optimal working temperature of 200°C.

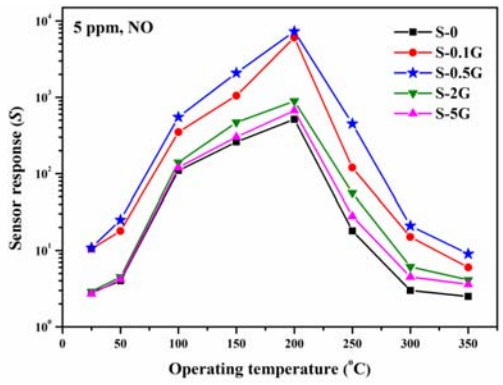

Figure 5. shows the plot of sensor response to 5 ppm of NO of pure SnO_2, and graphene-loaded SnO_2 sensors with different graphene loading levels (S-0, S-0.1G to S-5G) versus operating temperature ranging from 25 to 350°C.

The roles of graphene loading level on the NO-sensing performances at the optimal operating temperature of SnO_2 nanoparticles (S-0 and S-0.1G-S-5G) are evaluated with varying NO concentrations from 0.125 to 5 ppm as demonstrated in Figure 6(a). It can be observed that the baseline resistances of SnO_2 sensing films reduce monotonically with increasing graphene loading concentration from 0 to 5 wt%. After NO exposure, it is evident that the resistances of all sensors rise rapidly, indicating a typical *n*-type semiconducting behavior towards an oxidizing gas. Moreover, the change of resistance of SnO_2 sensor tends to enhance at low graphene-loading concentration (0.1-0.5 wt%) and then declines at higher graphene contents. Figure 6(b) displays the corresponding sensor response (solid line, left axis) and response time (dash line, right axis) of S-0 to S-5G sensors as a function of NO concentration. It is apparent that the sensor response and response time improve substantially with the elevation of graphene content from 0.1 to 0.5 wt %and then deteriorate considerably at higher graphene loading levels. Specifically, the S-0.5G sensor shows relatively high sensing performances in terms of response (S = 7,275) and response time (t_{res} = 61.3 s) at 5 ppm NO compared with S-0.1G (S = 6,071, t_{res} = 97.2 s), S-2G (S = 891, t_{res} = 106.2 s),S-5G (S = 669, t_{res} = 132.7 s) and S-0 (S = 514, t_{res} = 185.6 s). The attained NO response of <“7,275 at 5 ppm is much greater than most of other highly sensitive NO sensors, whose response values are less than 2000 to 5 ppm of NO as listed in Table 1. Additionally, the response characteristics as a function of NO concentration of graphene-loaded SnO_2 sensors conform to the well-known power law with exponent values of less than 1. Moreover, S-0.5G still exhibits a good NO response of ~13.45 at the low NO concentration of 0.125ppm. The detection limit of the optimal sensor is estimated by the power-law fitting method to be low as 10 ppb at the threshold response of 1.1. Therefore, the optimal graphene-loaded SnO_2 sensor is highly potential for

ultrasensitive NO detection at the low working temperature of 200°C.

The selectivity of graphene loaded SnO_2 sensing films were assessed towards 5 ppm NO, 5 ppm NO_2, 5 ppm H_2S, 2500 ppm H_2, 2000 ppm C_3H_6O and 2500 ppm CH_4 at the optimal operating temperatures of 200°C as demonstrated in Figure 7. It is seen that unloaded SnO_2 sensors display similarly high responses to NO and NO_2, medium response to H_2 and low response to other gases indicating relatively low NO selectivity against NO_2. With graphene loading, the NO response increases greatly at the optimal graphene content of 0.5 wt% while the responses to NO_2 and other gases only slightly increases. Thus, the NO response becomes the highest at the optimal graphene concentration of 0.5 wt % and the optimal graphene-loaded SnO_2 sensor offers not only ultrahigh response but also high NO selectivity against NO_2, H_2S, H_2, C_3H_6O and CH_4.

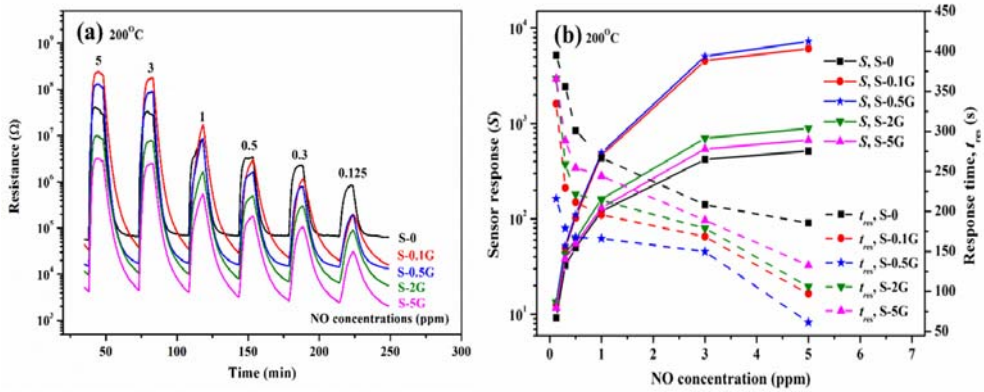

Figure 6(a). Change in resistance, (b) correlation of sensor response (solid line, left axis) and response time (dash line, right axis) vs nitric oxide concentration of S-0 to S-5G sensors at 200°C.

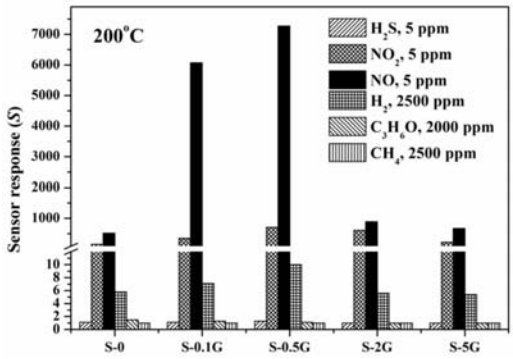

Figure. 7 shows selectivity histograms of sensor responses to 5 ppm of H_2S, NO_2, NO, 2500 ppm H_2, 2000 ppm C_3H_6O and 2,500 ppm $CH_4$of fabricated sensors (S-0, S-0.1G to S-5G) at the optimal operating temperature of 200°C.

3.3 NO Sensing Mechanisms of Graphene-loaded SnO_2 Nanoparticles

The substantial gas-sensing enhancement by graphene may be explained based on the following mechanisms. Firstly, graphene can offer additional surface area for adsorption sites and oxidizing reaction with NO, taking electrons from the conduction band to form chemisorbed *NO*$^-$ species and induce extended depletion regions. The formation of interfaces between graphene and SnO_2 nanoparticles could lead to additional active gas-adsorption sites (such as vacancies, point defects, oxygen functional groups as well as the sp^2-bonded carbon) because of chemical interaction between surface atoms of two

materials [22-24]. In addition, the gas-sensing enhancement by graphene may be ascribe to the metal-semiconductor (M-S) junction formed at the interface between SnO_2 and graphene. The graphene-loaded SnO_2 M-S junctions would induce reduction layers because of their work function difference in addition to the first depletion region formed on the surface of SnO_2 nanoparticles by chemisorbed oxygen species (O^- and O^{2-}) in air [6, 10]. The interaction between NO molecules and the surface of SnO_2 nanoparticles may enhance the first depletion layer while other NO molecules may also adsorb on graphene and extract electrons to expand the depletion layers at the graphene-loaded SnO_2 interfaces [19]. Therefore, the electronic interaction between SnO_2 and graphene effectively facilitates the NO detection via the alteration in the electrical conductivity of the hybrid nanostructure. Nevertheless, more theoretical and experimental studies are needed to verify this hypothesis. The surface accessibility between FSP-made nanoparticles and graphene also plays the key role to the enhanced response because the operation involves adsorption/desorption processes at the interface. Thus, the graphene-loaded SnO_2 system as a sensing element is potentially superior to either of its constituents.

Moreover, graphene could prevent agglomeration of SnO_2 nanoparticles though the intercalation effect as previously observed in SEM images (Figure 4 (c, g)), resulting in large effective surface area and substantially improved gas-sensing performances. Additionally, graphene's high electrical conductivity can contribute to the fast transport of electrons from gas interaction in the sensing layer, leading to the decrease of response and recovery times. The loading of conductive graphene into SnO_2 sensing films should enhance the material conductivity and electron transport since graphene is zero-band gap metal with very high electron mobility [6, 12]. From the results, the NO response of undoped SnO_2 sensing film is the highest at the optimal graphene loading level of 0.5 wt% but then considerably declines at higher graphene loading concentrations. This unexpected result may be explained from the SEM observation (Figure 4 (d, f)) that graphene sheets aggregate among themselves at high graphene loading levels. The aggregation of graphene sheets is due to strong Vanderwaal interactions between sp^2 layers and will always occur regardless of graphene quality. As the graphene sheets agglomerate, the quality will be degraded but they still exhibit metallic nature having very low resistance with a large number of electrons, which is far greater than that the amount of electrons that will be withdrawn by NO^- adsorption. Thus, the aggregated graphene sheets will form low-resistance conduction paths resulting in lower gas response.

Furthermore, the graphene-loaded SnO_2 sensors exhibit the optimal NO response at a relatively low working temperature of 200°C. This behavior can be attributed the temperature dependence of NO^- and O^- chemisorption on the material surface. The adsorption of O^- is very low at low temperatures ≤ 200°C so that there will a large number of available sites for NO^- chemisorption on the graphene/SnO_2 surface and more NO^- species can be adsorbed by the thermal activation with increasing temperature [25]. At higher working temperature, preadsorbed O^- species will be formed progressively with increasing temperature. As a result, there will be less accessible sites for NO^- chemisorption, leading to the decline of NO response at temperatures higher than 200°C.

4. CONCLUSIONS

FSP-made SnO_2 nanoparticles-loaded with electrolytically exfoliated graphene sheets (0.1-5wt%G) were systematically studied for NO sensing applications. The structural properties were analyzed by XRD, HR-TEM and SEM analyses, confirming the dispersion of multi-layer graphene sheets within SnO_2 nanoparticles. From gas-sensing measurements, the highest NO response was attained with the optimal graphene loading level of 0.5 wt% at the optimal operating temperature of 200°C. The 0.5 wt% graphene-loaded SnO_2 sensor exhibited notably high response of ~7,275 to 5 ppm NO with response time of 61.3 s at 200°C and high selectivity against NO_2, H_2, C_3H_6O, H_2S and CH_4. Therefore, the graphene-loaded SnO_2 sensor is a promising candidate for highly sensitive and selective NO detections in biomedical applications.

ACKNOWLEDGEMENTS

The authors gratefully acknowledge the financial support from Thailand Graduate Institute of Science and Technology (TGIST) (SCA-CO-2558-1039-TH, TG-44-10-58-018M), National Science and Technology Development Agency (NSTDA). We wish to thank the National Research University (NRU) Project under Thailand's Office of the Higher Education Commission for financial support, National Research Council of Thailand (NRCT), Thailand Research Fund (TRF) (RSA6080014, IRG5780013), Center of Excellence (CoE), Graduate School, Materials Science Research Center, Department of Physics and Materials Science, Faculty of Science, Chiang Mai University. The special thanks should be given to the National Electronics and Computer Technology Center (NECTEC), Pathumthani, Thailand for the sensor facilities.

REFERENCES

[1] Wang S.H., Shen C.Y., Lien Z.J. and Wang J.H., *Sen. Actuators B Chem.*, 2017; **243**: 1075-1082. DOI 10.3390/s150407084.

[2] Vilar M.R., El-Beghdadi J., Debontridder F., Naaman R., Arbel A., Ferraria A.M. and Do Rego A.M.B., *Mater. Sci. Eng. C*, 2006; **26(2-3)**: 253-259. DOI 10.1016/j.msec.2005.10.064.

[3] Dweik R., Boggs P., Erzurum S. and Irvin C., *Am. J.*, 2011; **184(1)**: 1-33. DOI 10.1164/rccm.9120-11ST.

[4] Ang G.T., Toh G.H., Zailani M., Bakar A. and Abdullah A.Z., *Process Saf. Environ. Prot.*, 2010; **89(3)**: 186-192. DOI 10.1016/j.psep.2010.10.008.

[5] Chikhale L.P., Patil J.Y., Rajgure A.V., Shaikh F.I., Mulla I.S. and Suryavanshi S.S., *Ceram. Int.*, 2014; **40(1)**: PART B, 2179-2186. DOI 10.1016/j.ceramint.2013.07.136.

[6] Schedin F., Geim A., Morozov S.V., Hill E.W., Blake P., Katsnelson M.I. and Novoselov K.S., *Nat. Mater.*, 2007; **6(9)**: 652-5. DOI 10.1038/nmat1967.

[7] Huang X., Yin Z., Wu S., Qi X., He Q., Zhang Q., Yan Q., Boey F. and Zhang H., *Small*, 2011; **7(14)**: 1876-1902. DOI 10.1002/smll.201002009.

[8] Li H.Y., Cai Z.X., Ding J.C. and Guo X., *Sen. Actuators, B Chem.*, 2015; **220**: 398-405. DOI 10.1016/j.snb.2015.05.091.

[9] Zhao J., Tan R., Shen W., Yang Y., Guo Y., Li J., Zhou Z., Jian J. and Song W., *Mater. Lett.*, 2012; **84(16)**: 94-96. DOI 10.1016/j.matlet.2012.06.048.

[10] Canevali C., Mari C.M., Mattoni M., Morazzoni F., Ruffo R., Scotti R., Russo U. and Nodari L., *Sen. Actuators B Chem.*, 2004; **100(1-2)**: 228-235. DOI 10.1557/PROC-828-A4.7.

[11] Lv T., Chen Y., Ma J. and Chen L., *RSC Adv.*, 2014; **4(43)**: 22487-22490. DOI 10.1039/C4RA03121K.

[12] Punginsang M., Wisitsora-At A., Tuantranont A., Phanichphant S. and Liewhiran C., *Sen. Actuators B Chem.*, 2015; **210**: 589-601. DOI 10.1016/j.snb.2015.01.028.

[13] Wang J., Rathi S., Singh B., Lee I., Maeng S., Joh H. and Kim G., *Sen. Actuators B Chem.*, 2015; **220**: 755-761. DOI 10.1016/j.snb.2015.05.133.

[14] Singh G., Choudhary A., Haranath D., Joshi A.G., Singh N., Singh S. and Pasricha R., *Carbon*, 2012; **50(2)**: 385-394. DOI 10.1016/j.carbon.2011.08.050.

[15] Akamatsu T., Itoh T., Izu N., Shin W. and Sato K., *Sensors*, 2015; **15(4)**: 8109-8120. DOI 10.3390/s150408109.

[16] Inyawilert K., Wisitsoraat A., Sriprachaubwong C., Tuantranont A., Phanichphant S. and Liewhiran C., *Sen. Actuators B Chem.*, 2014; **209**: 40-55. DOI 10.1016/j.snb.2014.11.086.

[17] Singkammo S., Wisitsoraat A., Sriprachuabwong C., Tuantranont A., Phanichphant S. and Liewhiran C., *ACS Appl. Mater. Interfaces*, 2015; **7(5)**: 3077-3092. DOI 10.1021/acsami.5b00161.

[18] Zhang H., Feng J., Fei T., Liu S. and Zhang T., *Sen. Actuators B Chem.*, 2014; **190(2)**: 472-478. DOI 10.1016/j.snb.2013.08.067.

[19] Kun P., Wéber F. and Balázsi C., *Cent. Eur. J. Chem.*, 2011; **9(1)**: 47-51. DOI 10.2478/s11532-010-0137-5.

[20] Ferrari A.C., *Solid State Commun.*, 2007; **143(1-2)**: 47-57. DOI 10.1016/j.ssc.2007.03.052.

[21] Lee G., Yang G., Cho A., Han J.W. and Kim J., *Phys. Chem. Chem. Phys.*, 2016; **18(21)**: 14198-14204. DOI 10.1039/C5CP04422G.

[22] Kundu S., Choudhury A., Mursalin S.M., Narjinary M. and Manna R., *J. Mater. Sci. Mater. Electron.*, 2015; **26(8)**: 6252-6260. DOI 10.1007/s10854-015-3211-0.

[23] Brunauer S., Emmett P.H. and Teller E., *J. Am. Chem. Soc.*, 1938; **60(1)**: 309-319. DOI 10.1021/ja01269a023.

[24] Rafiee J., Mi X., Gullapalli H., Thomas A.V., Yavari F., Shi Y., Ajayan P.M. and Koratkar N.A., *Nat. Mater.*, 2012; **11(3)**: 217-222. DOI 10.1063/1.4895541.

[25] Yamazoe N., Fuchigami J., Kishikawa M. and Seiyama T., *Surf. Sci.*, 1979; **86**: 335-344. DOI 10.1016/0039-6028(79)90411-4.